Robust Type-II Weyl Semimetal Phase in Transition Metal Diphosphides XP_2 (X = Mo, W)

G. Autès,[1,2] D. Gresch,[3] M. Troyer,[3] A. A. Soluyanov,[3,4] and O. V. Yazyev[1,2]

[1] *Institute of Physics, Ecole Polytechnique Fédérale de Lausanne (EPFL), CH-1015 Lausanne, Switzerland*
[2] *National Center for Computational Design and Discovery of Novel Materials MARVEL, Ecole Polytechnique Fédérale de Lausanne (EPFL), CH-1015 Lausanne, Switzerland*
[3] *Theoretical Physics and Station Q Zurich, ETH Zurich, 8093 Zurich, Switzerland*
[4] *Department of Physics, St. Petersburg State University, St. Petersburg, 199034 Russia*

(Dated: June 28, 2016)

The recently discovered type-II Weyl points appear at the boundary between electron and hole pockets. Type-II Weyl semimetals that host such points are predicted to exhibit a new type of chiral anomaly and possess thermodynamic properties very different from their type-I counterparts. In this Letter, we describe the prediction of a type-II Weyl semimetal phase in the transition metal diphosphides MoP_2 and WP_2. These materials are characterized by relatively simple band structures with four pairs of type-II Weyl points. Neighboring Weyl points have the same chirality, which makes the predicted topological phase robust with respect to small perturbations of the crystalline lattice. In addition, this peculiar arrangement of the Weyl points results in long topological Fermi arcs, thus making them readily accessible in angle-resolved photoemission spectroscopy.

arXiv:1603.04624v2 [cond-mat.mes-hall] 25 Jun 2016

Topological semimetals host band degeneracies in the vicinity of the Fermi level (E_F) that are associated with certain integer-valued topological invariants [1–9]. Since these invariants cannot continuously change their values, the associated degeneracies are protected against perturbations. One such semimetal phase – the Weyl semimetal (WSM) – hosts point-like linear band crossings of two bands with linear dispersion, the so-called Weyl points (WPs), in the vicinity of E_F. These WPs represent sources or sinks of Berry curvature, and their associated topological invariant is the Chern number $\mathcal{C} = \pm 1$ computed on a surface in momentum space that encloses the WP. Positive (negative) Chern numbers correspond to a source (sink) of the Berry curvature. A variety of topology-driven physical phenomena is predicted and observed in WSMs, ranging from the observation of open Fermi arcs in the surface spectrum [2, 10] to the realization of the chiral anomaly of quantum field theory [11–17].

It was recently shown [18] that unlike standard Lorentz-invariant field theory, condensed matter physics has two distinct types of Weyl fermions, and hence WSMs. While standard type-I Weyl fermions with closed Fermi surfaces were discovered in materials of the TaAs family [8, 9, 19–25], the novel type-II Weyl fermions appear at the boundary between electron and hole pockets, leaving an open Fermi surface which results in the anisotropic chiral anomaly [18, 26]. Two representatives of type-II WSMs materials considered to date are the orthorhombic low-temperature phases of WTe_2 and $MoTe_2$ [18, 27–29]. Type-II Weyl points were also recently predicted to exist in strained HgTe [30]. Eight (four) type-II WPs appear in WTe_2 ($MoTe_2$) formed by the valence and conduction bands. In WTe_2 some of the carrier pockets become topologically non-trivial, while in $MoTe_2$ they are all trivial, and the two materials represent very different Fermi arc arrangements [18, 28]. In both cases, however, the band structure is very complicated and the arrangement of WPs is sensitive to small changes in the crystal structure, which, in turn, is sensitive to temperature [27, 28]. Moreover, the proximity of WPs with opposite Chern numbers in k-space, as well as the existence of crossings between bands other than the topmost valence and the lowest conduction, at energies close to that of the WPs, makes the experimental confirmation of the type-II Weyl phase in WTe_2 and $MoTe_2$ a challenging task. The identification of materials with stable and easily observable type-II WPs thus sets an important problem in the study of this new topological phase.

In this Letter, we predict the existence of the type-II WSM phase in the previously synthesized compounds MoP_2 and WP_2. The crystal structure of these compounds is different from the previously reported ditellurides, resulting in a simpler band structure around E_F and a peculiar arrangement of WPs with nearest nodes characterized by the same Chern numbers, thus being stable against annihilating each other upon small lattice perturbations. This stability results in the presence of robust clearly visible long Fermi arcs at the surfaces of these compounds, which we expect to be readily observable in angle-resolved photoemission spectroscopy (ARPES) experiments.

The two compounds were identified by performing a high-throughput screening of the band structure topology of materials in the Inorganic Crystal Structure Database (ICSD) [31], using the hybrid Wannier charge center technique [32, 33] as implemented in the Z2Pack package [34]. Both MoP_2 and WP_2 crystallize in an orthorhombic base-centered structure [35, 36] containing two formula units per unit cell as shown in Fig. 1a. Both crystals are non-centrosymmetric and belong to the non-

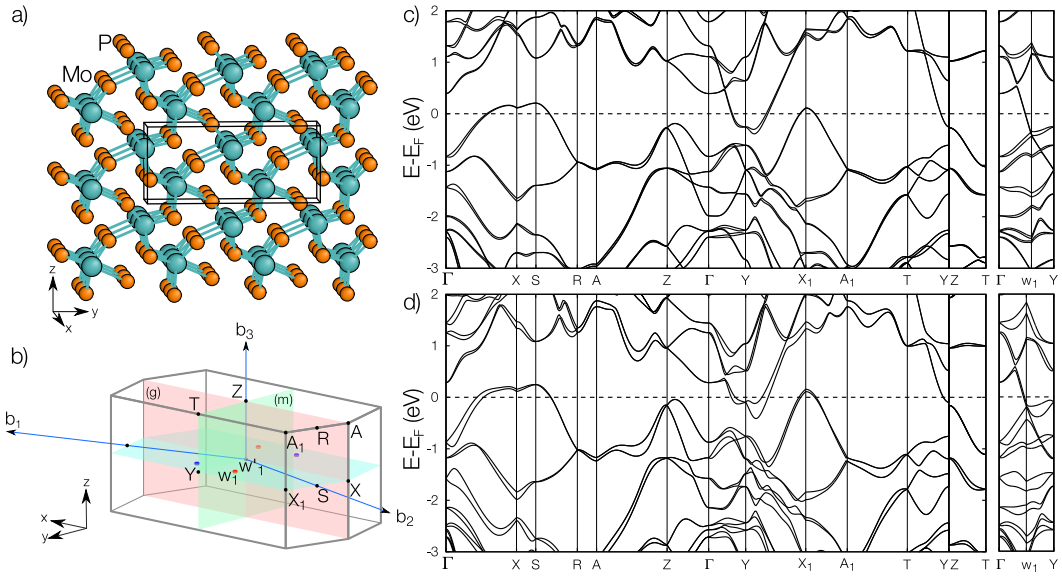

FIG. 1. (a) Crystal structure of MoP_2. The black box correspond to the orthorhombic conventional unit cell. (b) Brillouin zone of MoP_2 showing the positions of Weyl nodes with positive (red) and negative (blue) Chern numbers. Band structures of (c) MoP_2 and (d) WP_2 plotted along high symmetry directions, as well as along the $\Gamma w_1 Y$ path in order to reveal the band crossings.

symmorphic space group $Cmc2_1$ (36), which contains three symmetries: a C_2 screw axis along the [001] direction (2_1), a mirror plane normal to the [100] direction (m, shown in green in Fig. 1b), and a glide plane normal to the [010] direction (g, shown in red in Fig. 1b). Although the crystalline symmetries of MoP_2 and WP_2 are similar to that of the ditellurides, the atomic structure of the phosphides is very different. While the structure of XTe_2 consist of van der Waals bonded layers, no layered structure exists in XP_2 materials.

The electronic structure of MoP_2 and WP_2 was computed from first principles [37, 38]. The methodology is described in more detail in the Supplemental Material [1]. The band structures along the high-symmetry directions of the Brillouin zone (BZ) are shown in Fig. 1c and 1d, for MoP_2 and WP_2, respectively. Both compounds share a similar semimetallic band structure, very different from that of the XTe_2 compounds, with an electron pocket around Y and a hole pocket in the vicinity of the XS direction. The Fermi contour of these pockets is shown with a dashed line in Fig. 2a for MoP_2 at $k_z = 0$. The main difference between the two compounds is that the spin-orbit coupling (SOC) is stronger in WP_2, which results in a larger band splitting compared to MoP_2.

The band structure of MoP_2 and WP_2 along the high symmetry lines of the BZ suggests that these compounds are ordinary semimetals. However, a more careful analysis reveals the presence of eight points in the $k_z = 0$ plane where conduction and valence bands touch. This can be seen in Fig. 2a, where we plot the energy difference between the lowest conduction and the highest valence bands in the $k_z = 0$ plane of the BZ. The gap closes at two inequivalent points w_1 and w_1', located away from any high-symmetry line. The positions of these points are listed in Table I. The six other points w_i and w_i' ($i = 2, 3, 4$) are related to w_1 and w_1' by mirror and time-reversal ($\mathcal{T}$) symmetries. In both compounds, w_1 and w_1' are at -0.410 eV and -0.364 eV relative to the Fermi level in MoP_2 and at -0.471 eV and -0.340 eV relative to the Fermi level in WP_2.

Analogously to the case of XTe_2, the existence of degeneracy points in the $k_z = 0$ plane of MoP_2 and WP_2 is due to the presence of the product symmetry $C_2\mathcal{T}$, which restricts a general 2×2 Hamiltonian in the plane to be of the form

$$\mathcal{H}(k_x, k_y, 0) = d_0(k_x, k_y)\sigma_0 + d_y(k_x, k_y)\sigma_y + d_z(k_x, k_y)\sigma_z, \quad (1)$$

where $\sigma_{y,z}$ are the corresponding Pauli matrices and σ_0 is the 2×2 unit matrix associated with the kinetic energy term of the type-II Weyl Hamiltonian [18]. The full derivation of the model Hamiltonian is presented in the Supplemental Material [1]. In order to establish that the

TABLE I. Positions, Chern numbers and energies of the Weyl points in MoP_2 and WP_2.

		k_x (Å^{-1})	k_y (Å^{-1})	Chern number $\mathcal{C}$	$E - E_F$ (eV)
MoP_2	w_1	−0.2010	0.3627	+1	−0.410
MoP_2	w_1'	−0.1939	0.3516	+1	−0.364
WP_2	w_1	−0.2627	0.3165	+1	−0.471
WP_2	w_1'	−0.2577	0.2818	+1	−0.340

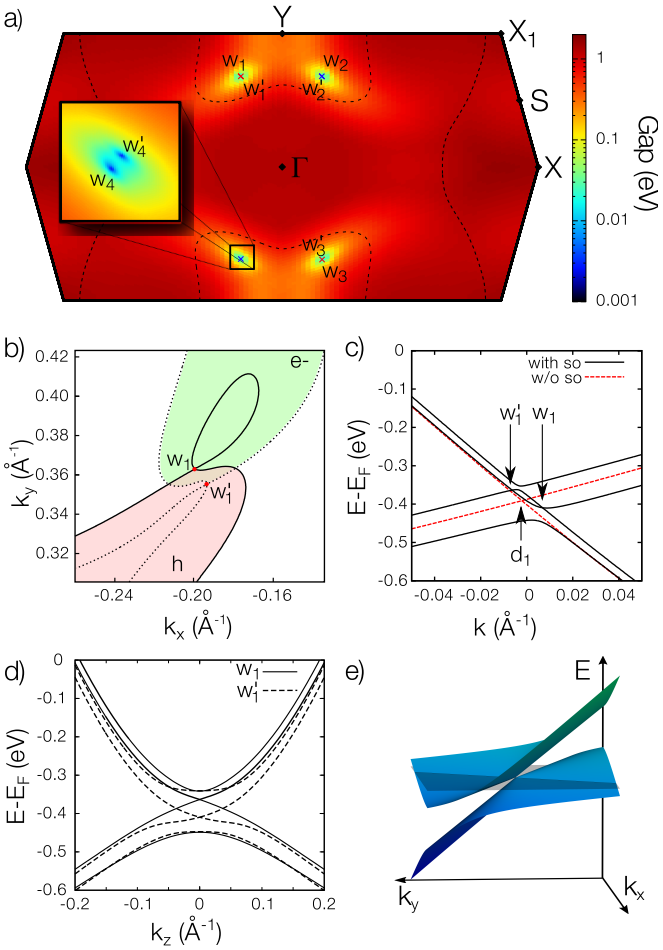

FIG. 2. (a) Energy difference between the lowest conduction band and the highest valence band of MoP_2 in the $k_z = 0$ plane of the Brillouin zone. The crosses correspond to the 8 Weyl nodes with Chern numbers $\mathcal{C} = +1$ (red) and -1 (blue). The dashed lines show the contours of the hole and electron pockets at the Fermi level in the $k_z = 0$ plane. (b) Constant energy contour of the MoP_2 hole (red) and electron (green) pockets in the $k_z = 0$ plane at the energy of w_1 (continuous line) and of w_1' (dashed line). (c) Band structure of MoP_2 along the $w_1 w_1'$ line in the $k_z = 0$ plane with (black) and without (red) spin-orbit coupling. (d) Band structure of MoP_2 along k_z at k_x and k_y corresponding to the Weyl points w_1 (continuous line) and w_1' (dotted line). (e) Energy dispersion around the type-II Weyl point w_1 in the $k_z = 0$ plane.

degeneracies w_i and w_i' are indeed WPs, we computed the Chern numbers of surfaces enclosing these points following the method described in Ref. [18]. We find that both w_1 and w_1' carry a topological charge $\mathcal{C} = +1$ [1], while the charges of the other six points are obtained by symmetry arguments: mirror reflection flips the sign of the Chern number of a WP, thus $w_{2,4}$ and $w_{2,4}'$ have $\mathcal{C} = -1$, while $\mathcal{T}$-reflection preserves it, so $\mathcal{C} = +1$ for w_3 and w_3'.

The WPs in MoP_2 and WP_2 are of type-II as can be concluded by examining the Fermi surface at the energies of w_1 and w_1', shown in Fig. 2b for the case of MoP_2. Both nodes appear at the points of contact between the electron pocket located around Y and the hole pocket located along the XS direction. To further confirm this conclusion, we fitted the *ab initio* band structure in the vicinity of the WPs to find the coefficients d_i of Eq. 1 to the linear order in $\mathbf{k}$ [1]. For both the w_1 and w_1' points, the kinetic term dominates the spectrum along the k_y direction around the WP, as illustrated in Fig. 2e for the WP w_1. The dominant kinetic term in the k_y direction suggests a possible observation of the type-II chiral anomaly [18] in XP_2 compounds when both electric and magnetic fields are applied along this direction.

The WPs w_1 and w_1' are separated in energy. To understand the origin of this separation, we note that the two points are formed by spin-split bands, as can be concluded from Fig. 2c and Fig. 2d, where the energy dispersion of MoP_2 is shown along a path connecting the two WPs in the $k_z = 0$ plane and along the k_z direction, respectively. Indeed, for a calculation performed without taking into account SOC, the electron and hole pockets touch at 4 crossing points d_i in the $k_z = 0$ plane, which have the associated topological charge $\mathcal{C} = \pm 2$ and correspond to the superposition of two WPs of the same chirality, as expected for SU(2) symmetry [40]. These double WPs are split by the SOC into single nodes w_i and w_i' (see Fig. 2c) that have the same chirality.

The magnitude of the splitting in energy and k-space between the two adjacent WPs w_i and w_i' is hence directly related to the strength of the SOC. These splittings are larger in WP_2 (131 meV and 0.035 $Å^{-1}$) than in MoP_2 (46 meV and 0.013 $Å^{-1}$) (see Table I), as expected due to the larger SOC strength in W. This suggests the possibility of tuning the separation between the WPs in these compounds in both energy and momentum by applying strain or chemical substitution, since this changes the effective SOC.

Unlike the case of ditellurides, the neighboring WPs in XP_2 materials have the same chirality, and thus cannot annihilate each other. This implies that MoP_2 and WP_2 realize a stable type-II WSM phase that is far from a possible topological phase transition caused by a merging of the opposite chirality WPs. Opposite chirality WPs can annihilate when they reach the same point of the 3D BZ, so the smallest distance in k-space between WPs with opposite Chern number $\mathcal{C}$ can be considered as a measure of stability of the WSM phase. We find this distance to be $0.38Å^{-1}$ and $0.52Å^{-1}$ in MoP_2 and WP_2, respectively, which constitutes 20% and 26% of the corresponding inverse lattice constants. These numbers can be compared to the distance between opposite chirality WPs in the TaAs materials family, in particular TaP where the distance is the longest[8] and is $0.09Å^{-1}$ (4% of the inverse lattice constant). The distance between the neighboring opposite chirality WPs in XTe_2 is 0.7% of the inverse

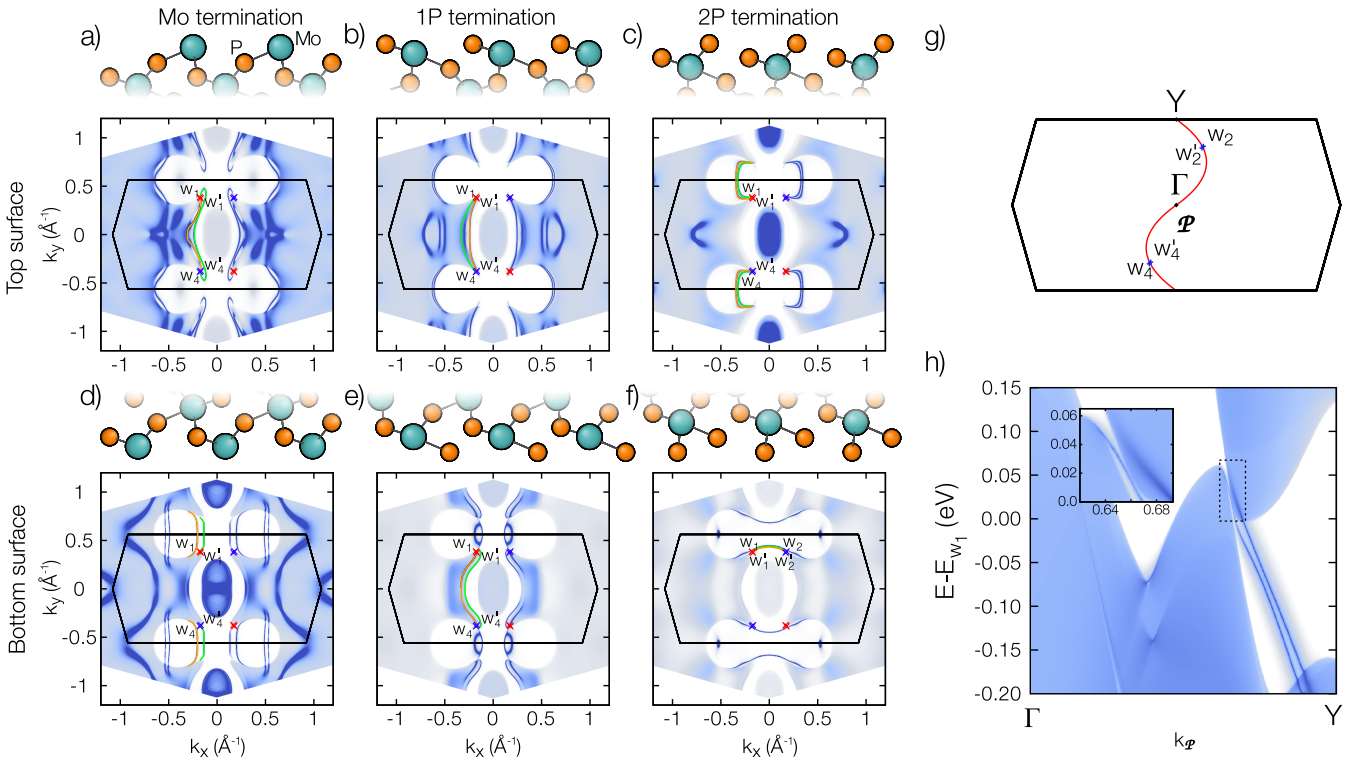

FIG. 3. Surface density of states of (a,b,c) the top and (d,e,f) the bottom (001) surfaces with Mo- and P-terminations 1P and 2P at the energy of the Weyl node w_1. The green and orange lines indicate the topological Fermi arcs connecting the w_i and w_i' WPs, respectively. (g) Cut in the $k_z = 0$ plane of the $\mathcal{T}$-symmetric plane $\mathcal{P}$ with $\mathbb{Z}_2$ invariant 1. (h) Surface density of states of the top P-terminated surface 2P along $\mathcal{P}$ from Γ to Y. The inset panel shows a magnified view of the region in proximity of the hole and electron pockets. Only one of the two surface states is topological, connecting the electron and hole pockets.

lattice constant.

One evident consequence of the large k-space separation of opposite chirality WPs in XP_2 is the possibility of the observation of extended topological Fermi arcs in the surface of these materials. For type-I WPs, which have a point-like Fermi surface, these Fermi arcs connect the projections of the opposite chirality WPs onto the surface. In contrast, the Fermi surface of the type-II WPs is open and the projection of the points is generally hidden within the projection of a charge-carrier pocket.

We consider the (001) surface of MoP_2 and WP_2, since the eight WPs project onto distinct points of the corresponding surface BZ, allowing for the observation of Fermi arcs. We find that at all energies all electron and hole pockets enclose an equal number of chiral and antichiral WPs, therefore the Chern number of all these pockets vanishes. From this perspective, no Fermi arcs connecting electron and hole pockets are expected. Indeed, at E_F we find that the projected WPs are covered by the projection of the electron pocket around the Y point and no Fermi arcs can be observed. However, we do find topological Fermi arcs in these materials at lower energies as we explain below.

We computed the surface density of states of MoP_2 using the tight-binding model, obtained from the bulk Wannier functions [41] for Mo d and P p orbitals, in order to compute the Green's function of the semi-inifnite surface according to the method introduced in Ref. [42]. Three possible surface terminations were investigated: one Mo-terminated and two P-terminated denoted as 1P and 2P. Furthermore, the top and bottom (001) surfaces of MoP_2 are inequivalent, thus giving rise to six different configurations (see Fig. 3a–f). The surface densities of states at the energy of w_1, 0.41 eV below E_F, all show two distinct Fermi arcs. One of these arcs connects two w_i points of opposite chirality (green line in Fig. 3a–f), while the other one connects two w_i' points of opposite chirality (orange line in Fig. 3a–f). Both the connectivity and the shape of the Fermi arcs depend on the details of the surface termination. For the Mo and 1P top surfaces as well as for the 1P bottom surface, the Fermi arcs connect w_1 (w_1') and w_4 (w_4') within the surface BZ, which is shown as black hexagon in Fig. 3. On the 2P top surface and the Mo bottom surface w_1 (w_1') is connected by a Fermi arc to w_4 (w_4') across the surface BZ boundary. Finally, on the 2P bottom surface, the Fermi arcs connect the w_1 (w_1') and w_2 (w_2') WPs.

While the connectivity of these Fermi arcs depends on a particular surface, one can argue that the arcs themselves are of topological origin. In order to demonstrate

this we computed the $\mathbb{Z}_2$ invariant on the $\mathcal{T}$-symmetric plane $\mathcal{P}$ shown in Fig. 3g and find it to be non-trivial (see Supplemental Material for details [1]). This implies that this cut of the BZ, on which the spectrum is gapped at all points, is a quantum spin Hall effect system [43], and therefore it is guaranteed to show topologically protected edge states. In other words, any line cut of the (001) surface BZ that passes between the two WPs has to cross a topological Fermi arc as shown in Fig. 3h. The conclusion that the Fermi arcs connecting points w_i and w_i' are of topological origin agrees with the values of $\mathbb{Z}_2$ invariants defined on different $\mathcal{T}$-symmetric planes of the BZ, as further discussed in the Supplemental Material [1].

The predicted Fermi arcs span extended regions of k-space and are localized below the Fermi level. Therefore they should be readily observable in ARPES experiments on a cleaved (001) surface of XP_2 compounds. Experimental observation of these arcs will provide an unambiguous evidence of the type-II Weyl fermions in these materials. It should be noted that other surface states are visible in Figs. 3a–f. A careful examination of the electronic structure shows that these states do not originate from Weyl points and are thus topologically trivial, as discussed in the Supplemental Material [1].

In conclusion, we theoretically identified a new family of type-II Weyl semimetals in the transition disphophides MoP_2 and WP_2. The Brillouin zone of these materials contains 4 pairs of Weyl nodes with the same chirality in the $k_z = 0$ plane, which implies robustness of the predicted Weyl semimetal phase. We predict that a type-II chiral anomaly should be observable in these compounds and that long Fermi arcs should be detectable by ARPES experiments on the [001] surface with a great variety of possible arrangements depending on the surface termination.

Acknowledgments G.A. and O.V.Y. acknowledge support by the NCCR Marvel and the ERC Starting grant "TopoMat" (Grant No. 306504). First-principles electronic structure calculations have been performed at the Swiss National Supercomputing Centre (CSCS) under project s515. D. G., A. A. S. and M. T. were supported by Microsoft Research, the European Research Council through ERC Advanced Grant SIMCOFE, and the Swiss National Science Foundation through the National Competence Centers in Research MARVEL and QSIT.

[1] G. E. Volovik, *The Universe in a Helium Droplet* (Oxford University Press New York, 2009).
[2] X. Wan, A. M. Turner, A. Vishwanath, and S. Y. Savrasov, Phys. Rev. B **83**, 205101 (2011).
[3] A. A. Burkov and L. Balents, Phys. Rev. Lett. **107**, 127205 (2011).
[4] Z. Wang, Y. Sun, X.-Q. Chen, C. Franchini, G. Xu, H. Weng, X. Dai, and Z. Fang, Phys. Rev. B **85**, 195320 (2012).
[5] S. M. Young, S. Zaheer, J. C. Y. Teo, C. L. Kane, E. J. Mele, and A. M. Rappe, Phys. Rev. Lett. **108**, 140405 (2012).
[6] Z. K. Liu *et al.*, Nat. Mater. **13**, 677 (2014).
[7] Z. K. Liu *et al.*, Science **343**, 864 (2014).
[8] H. Weng, C. Fang, Z. Fang, B. A. Bernevig, and X. Dai, Phys. Rev. X **5**, 011029 (2015).
[9] S.-M. Huang *et al.*, Nat. Commun. **6**, 7373 (2015).
[10] M. A. Silaev and G. E. Volovik, Phys. Rev. B **86**, 214511 (2012).
[11] H. Nielsen and M. Ninomiya, Phys. Lett. B **130**, 389 (1983).
[12] A. A. Zyuzin and A. A. Burkov, Phys. Rev. B **86**, 115133 (2012).
[13] P. Hosur and X. Qi, Comptes Rendus Phys. **14**, 857 (2013).
[14] G. E. Volovik, JETP Lett. **98**, 753 (2014).
[15] J. Xiong, S. K. Kushwaha, T. Liang, J. W. Krizan, W. Wang, R. J. Cava, and N. P. Ong, arXiv:1503.08179.
[16] C. Zhang *et al.*, arXiv:1503.02630.
[17] X. Huang *et al.*, Phys. Rev. X **5**, 031023 (2015).
[18] A. A. Soluyanov, D. Gresch, Z. Wang, Q. Wu, M. Troyer, X. Dai, and B. A. Bernevig, Nature **527**, 495 (2015).
[19] S.-Y. Xu *et al.*, Science **349**, 613 (2015).
[20] B. Lv *et al.*, Phys. Rev. X **5**, 031013 (2015).
[21] B. Q. Lv *et al.*, Nat. Phys. **11**, 724 (2015).
[22] L. X. Yang *et al.*, Nat. Phys. **11**, 728 (2015).
[23] S.-Y. Xu *et al.*, Nat. Phys. **11**, 748 (2015).
[24] N. Xu *et al.*, Nat. Commun. **7**, 11006 (2016).
[25] S.-Y. Xu *et al.*, Sci. Adv. **1**, e1501092 (2015).
[26] G. Volovik and M. Zubkov, Nucl. Phys. B **881**, 514 (2014).
[27] Y. Sun, S.-C. Wu, M. N. Ali, C. Felser, and B. Yan, Phys. Rev. B **92**, 161107 (2015).
[28] Z. Wang *et al.*, http://arxiv.org/abs/1511.07440 arXiv:1511.07440.
[29] T.-R. Chang *et al.*, Nat. Commun. **7**, 10639 (2016).
[30] J. Ruan, S.-K. Jian, H. Yao, H. Zhang, S.-C. Zhang, and D. Xing, arXiv:1511.08284.
[31] G. Bergerhoff, R. Hundt, R. Sievers, and I. D. Brown, J. Chem. Inf. Model. **23**, 66 (1983).
[32] A. A. Soluyanov and D. Vanderbilt, Phys. Rev. B **83**, 235401 (2011).
[33] R. Yu, X. L. Qi, A. Bernevig, Z. Fang, and X. Dai, Phys. Rev. B **84**, 075119 (2011).
[34] D. Gresch, A. A. Soluyanov, G. Autès, O. V. Yazyev, B. A. Bernevig, D. Vanderbilt, and M. Troyer, in preparation, package available at http://z2pack.ethz.ch/..
[35] S. Rundqvist and T. Lundström, Acta Chem. Scand. **17**, 37 (1963).
[36] R. Rühl and W. Jeitschko, Monatshefte fur Chemie Chem. Mon. **114**, 817 (1983).
[37] P. Giannozzi *et al.*, J. Phys. Condens. Matter **21**, 395502 (2009).
[38] A. Dal Corso and A. Mosca Conte, Phys. Rev. B **71**, 115106 (2005).
[1] See Supplemental Material at ... for the details of the first-principles calculations, the derivation of the full model Hamiltonian, the computation of topological invariants and a description of the additional Weyl points present in the valence band.
[40] Z. J. Wang, A. A. Soluyanov, M. Troyer, X. Dai, and B. A. Bernevig, in preparation..

[41] A. A. Mostofi, J. R. Yates, Y.-S. Lee, I. Souza, D. Vanderbilt, and N. Marzari, Comput. Phys. Commun. **178**, 685 (2008).
[42] A. Umerski, Phys. Rev. B **55**, 5266 (1997).
[43] C. L. Kane and E. J. Mele, Phys. Rev. Lett. **95**, 146802 (2005)

Supplemental Material for "Robust Type-II Weyl Semimetal Phase in Transition Metal Diphosphides XP_2 (X = Mo, W)"

I. METHODOLOGY

The electronic structure of MoP_2 and WP_2 was computed within the density functional theory (DFT) framework using the generalized gradient approximation (GGA) as implemented in QUANTUM-ESPRESSO software package [S1]. Spin-orbit coupling (SOC) is taken into account with the help of fully relativistic ultrasoft pseudopotentials [S2]. The calculations were carried out using an 885 k-point mesh and a planewave kinetic energy cutoff of 50 Ry for the wavefunctions. We used the experimentally determined crystal structure from Ref. [S3].

II. MODEL HAMILTONIAN OF THE WEYL POINTS

The general 2×2 Hamiltonian restricted by $C_2\mathcal{T}$ symmetry in the $k_z = 0$ plane is of the form [S4, S5]

$$\mathcal{H}(k_x, k_y, 0) = d_0\sigma_0 + d_y\sigma_y + d_z\sigma_z. \tag{S1}$$

The co-dimension of the system of equations defining a band gap closure ($d_y = d_z = 0$) is zero, meaning that stable nodal points can exist. The general linearized form of the Hamiltonian around a crossing point in the $k_z = 0$ plane is given by

$$\mathcal{H} = v_1k_x + v_2k_y + (ak_x + bk_y)\sigma_y + (ck_x + dk_y)\sigma_z + ek_z\sigma_x + \varepsilon_0, \tag{S2}$$

where the k_i are relative to the crossing point. The fitting parameters for the different Weyl points are given in Table S1. From these parameters, one can easily verify that all Weyl fermions are of type-II, as shown in Fig. 2e of the main text.

TABLE S1. Linear fit parameters of the Hamiltonian around the Weyl nodes in eV Å^{-1}.

	b	c	d	e	v_1	v_2
MoP_2 w_1	1.11	1.46	−1.82	−0.90	0.44	−2.6
MoP_2 w_1'	1.18	1.43	−1.32	−0.77	0.73	−2.99
WP_2 w_1	1.20	1.79	−1.29	−0.06	−0.47	−3.49
WP_2 w_1'	1.94	1.64	−2.16	−0.12	−0.91	−2.30

III. CHIRALITY OF THE WEYL NODES AND TOPOLOGICAL INVARIANTS

The chirality of the Weyl points w_i and w_i' was obtained by computing the flux of Berry curvature through a surface enclosing them. In order to carry out this calculation, we follow the method proposed by Ref. [S4]. We calculate Wannier charge centers on longitudinal loops around a sphere enclosing the Weyl point (see Fig. S1a). The sum of the Wannier charge centers on a loop with longitudinal angle θ_i corresponds to the Berry phase accumulated along the loop, or similarly to the average position $\langle\phi\rangle$ of the charge on the loop. When the angle θ varies from 0 to π, the loops cover a closed surface and the average position of center $\langle\phi\rangle$ can only be shifted by an integer number of 2π. This number correspond to the chirality of the Weyl node enclosed in the sphere.

We apply this procedure to a sphere enclosing w_1 (red curve, Fig. S1a). As the angle θ varies from 0 to π, the average position of the Wannier centers on the loops ($\langle\phi\rangle$) is shifted by 2π, which indicates that w_1 is a source of Berry curvature with chirality $\mathcal{C} = +1$. The Weyl node w_2, which is the mirror image of w_1, is then expected to carry a topological charge $\mathcal{C} = -1$. This is confirmed by the evolution of the WCC on a sphere enclosing w_2 (blue curve, Fig. S1a) The same method can be applied to show that the Weyl node w_1' has a chirality $\mathcal{C} = +1$ (see Fig. S1b).

To further elucidate the topological character of MoP_2 and WP_2, several topological invariants were computed from first-principles. The presence of time-reversal ($\mathcal{T}$) symmetry allows the computation of the $\mathbb{Z}_2$ invariant on

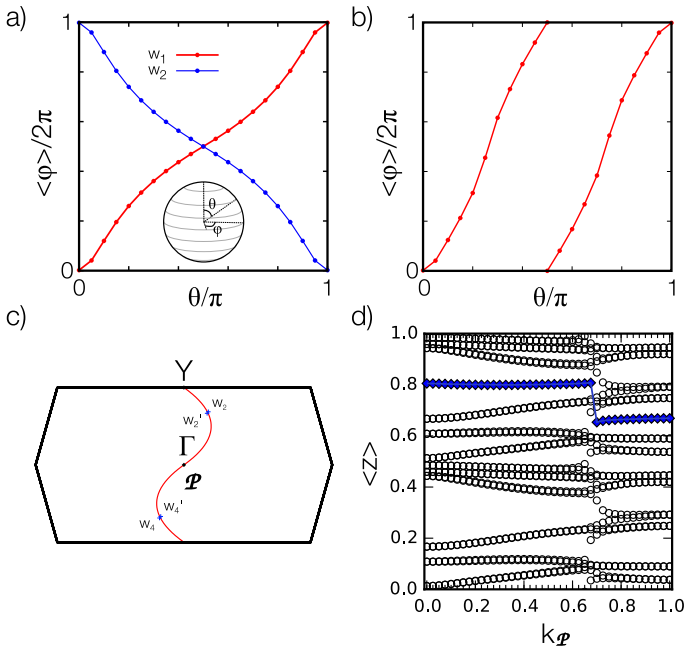

FIG. S1. a) Evolution of the Wannier charge centers on loops of longitudinal angle θ forming a sphere enclosing w_1 (red) and a sphere enclosing w_2 (blue) in MoP_2, b) Evolution of the Wannier charge centers on loops of longitudinal angle θ forming a sphere enclosing w_1 and w_1' (red) in MoP_2, d) Wannier charge centers $\langle z \rangle$ (black circle) along the half-plane $(\mathcal{C}, k_z)$ from Γ to Y shown in red in panel (c). The blue diamonds show the position of the largest gap which corresponds to a non-trivial $\mathbb{Z}_2$ invariant.

$\mathcal{T}$-symmetric planes in the BZ, defined by $k_i = 0, \pi$, where $i = x, y, z$. The $k_z = 0$ hosts WPs and does not have a well-defined invariant. For the other five planes, the topological invariant is computed using a hybrid Wannier centers technique [S6, S7] and found to be trivial. Nevertheless, it is still possible to define a non-trivial $\mathbb{Z}_2$ invariant [S8] by considering a curved $\mathcal{T}$-symmetric plane crossing between the w_1 and w_1' (or w_2 and w_2') and their $\mathcal{T}$ image w_3 and w_3' (or w_4 and w_4'). The path along which such a plane $\mathcal{P}$ cut the $k_z = 0$ plane is shown on Fig. S1c. The evolution of the Wannier charge centers positions on the half plane $\mathcal{P}$ from Γ to Y is shown on Fig. S1d which is not gapped and corresponds to a non-trivial $\mathbb{Z}_2$ invariant.

IV. ADDITIONAL TOPOLOGICAL FEATURES BELOW THE VALENCE BAND

An examination of the band structure plots along the ΓY and $Y X_1$ direction in Fig.1 of the main text, reveals that other non-trivial crossings exist between the bands below the valence and above the conduction band. In order to allow an easy experimental observation of the main WPs, it is important that such features are located sufficiently far in energy or k-space from the w_i and w_i' points. In the valence bands, 12 WPs corresponding to crossings between the $n-1$ and $n-2$ bands (where n is the number of valence electrons) are located in the $k_z = 0$ plane on each side of the ΓY line at ≈ 0.26 eV below the w_i WP. In the conduction band, 8 WPs corresponding to crossings between the $n+2$ and $n+3$ bands are located in the $k_z = 0$ plane at ≈ 0.8 eV above the w_i WP. The energies and position of these features show that the main WPs w_i and w_i' are well isolated from any others WPs. This provides a great advantage for the experimental characterization of the Weyl phase over other type-II WSM such as WTe_2 and $MoTe_2$.

Here, we describe additional topological features that appear below the valence band in MoP_2 and WP_2. The closest in energy to the Fermi level corresponds to crossing between the $n-1$ and $n-2$ bands (where n is the number of valence electron). 12 Weyl points formed by these bands are located in the $k_z = 0$ plane on each side of the ΓY line. The position of 3 inequivalent points x_1, x_2 and x_3 is shown on Fig. S2 for MoP_2. The 9 other points can be obtained by applying the mirror and time-reversal symmetries. The highest in energy of these points has an energy of -0.673 eV with respect to the Fermi level (see Table S2). They are thus separated from the lowest Weyl point w_i by an energy of ≈ 0.26 eV. The position in k-space and energy of the x_i points demonstrate that the main Weyl points w_i and w_i' are well isolated and that the additional surface states that appears in Fig. 3a–f of the main text are not

of topological origin.

TABLE S2. Positions and energies of the Weyl nodes between the $n-1$ and $n-2$ bands in MoP_2

	k_x (Å^{-1})	k$_y$ (Å^{-1})	$E - E_F$ (eV)
x_1	−0.0192	−0.2933	−0.684
x_2	−0.0923	−0.4465	−0.692
x_3	−0.0232	−0.4401	−0.673

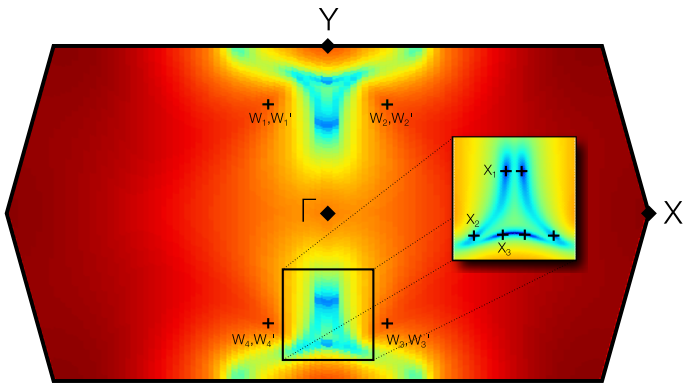

FIG. S2. Energy difference between the $n-1$ and $n-2$ bands in the $k_z = 0$ plane of MoP_2.

[S1] P. Giannozzi, S. Baroni, N. Bonini, M. Calandra, R. Car, C. Cavazzoni, *et al.*, J. Phys. Condens. Matter **21**, 395502 (2009).
[S2] A. Dal Corso and A. Mosca Conte, Phys. Rev. B **71**, 115106 ST (2005).
[S3] R. Rühl and W. Jeitschko, Monatshefte fur Chemie Chem. Mon. **114**, 817 (1983).
[S4] A. A. Soluyanov, D. Gresch, Z. Wang, Q. Wu, M. Troyer, X. Dai, and B. A. Bernevig, Nature **527**, 495 (2015).
[S5] Z. J. Wang, A. A. Soluyanov, M. Troyer, X. Dai, and B. A. Bernevig, in preparation..
[S6] A. A. Soluyanov and D. Vanderbilt, Phys. Rev. B **83**, 235401 (2011).
[S7] R. Yu, X. L. Qi, A. Bernevig, Z. Fang, and X. Dai, Phys. Rev. B **84**, 075119 (2011).
[S8] C. L. Kane and E. J. Mele, Phys. Rev. Lett. **95**, 146802 (2005)

[S1] See Supplemental Material at ... for the details of the first-principles calculations, the derivation of the full model Hamiltonian, the computation of topological invariants and a description of the additional Weyl points present in the valence band.